Available online at www.sciencedirect.com

jmr&t Journal of Materials Research and Technology

https://www.journals.elsevier.com/journal-of-materials-research-and-technology

Effect of laser welding on the mechanical and degradation behaviour of Fe-20Mn-0.6C bioabsorbable alloy

J. Fiocchi[a], C.A. Biffi[a,*], S. Gambaro[b], C. Paternoster[b], D. Mantovani[b], A. Tuissi[a]

[a] National Research Council, Institute of Condensed Matter Chemistry and Energy, CNR-ICMATE - Lecco, 23900, Italy

[b] Laboratory for Biomaterials and Bioengineering, CRC-I, Dept. Min-Met-Materials Engineering & CHU de Québec Research Center, Laval University, Quebec City G1V 0A6, Canada

ARTICLE INFO

Article history:
Received 23 August 2020
Accepted 24 September 2020
Available online 3 October 2020

Keywords:
Bioabsorbable metallic compounds
Laser welding
Fe-Mn alloys
Microstructure
Mechanical properties
In vitro degradation

ABSTRACT

The present work aims at exploring the influence of laser welding on the functional behaviour of a Fe-20Mn-0.6C (wt.%) bioabsorbable alloy. At first, the selection of the most suitable process speed (40 mm/s) was done in order to obtain a full penetration joint with limited taper. Then, microstructural and mechanical analyses of welded sheets confirmed suitable performance of the joint, without porosity, thus preserving chemical composition, mechanical resistance and ductility even after welding. In particular, the base material comprised both γ austenite and ε martensite, while the welded samples showed a further type of martensite, namely α'. Moreover, ultimate tensile strength (1095 MPa and 1104 MPa in base and welded material, respectively) and elongation to failure (61.3% and 60.9%, respectively) were almost not influenced by the welding process. Considering the absorbable nature of these alloys, static immersion degradation tests were carried out, and confirmed that the surface of the welded bead did not exhibit a significant variation of the material degradation rate after 14 days in modified Hanks' solution. Finally, a significant accumulation of degradation products, mainly $(Fe,Mn)CO_3$, was observed along the joining line.

1. Introduction

In the last years, large research efforts have been devoted to the development of bioabsorbable medical implants, which exhibit significant advantages over permanent ones. In fact, they do not need to be removed after implantation, fulfilling their expectation when implanted for as long as required, and then degrading and being eliminated by the physiological channels, thus also satisfying paediatric needs [1]. For this purpose, several materials, including polymers and metallic alloys (Mg, Zn and Fe-based ones) [2], have been developed and studied with the intent to reach the best compromise between mechanical properties, cytocompatibility and degradation rate. Among biodegradable alloys, the Fe-based ones display attractive properties from many different perspectives and they are thus widely studied as extremely promising candidates for biodegradable implants [3,4]. In particular, Fe-Mn-C alloys are characterized by an acceptable corrosion rate, as determined by static immersion degradation tests [5], an excellent biocompatibility [6,7] and high mechanical proper-

* *Corresponding author.*
E-mail: carloalberto.biffi@cnr.it (C. Biffi).

https://doi.org/10.1016/j.jmrt.2020.09.104

ties, which depend on the activation of different deformation mechanisms, including formation of twins and stress-induced martensite [8–11].

As the development of bioabsorbable metals is relatively recent, limited attention has been devoted so far to the development of effective manufacturing processes for biomedical devices, and in particular to the possible influence of welding on the behaviour of biodegradable implants. For example stents, which are widely diffused medical implants used for treating a variety of diseases including cardiovascular, cerebral and ureteral ones, are currently produced, in their permanent form, through different production routes. On one hand, production may start from the cast material and progress through different plastic deformation steps (e.g. extrusion and drawing) to obtain at first semi-finished products in the form of minitubes. The obtained tubes are then processed by laser cutting in order to achieve the desired mesh [12]; finally, they need to be heat treated and electropolished [13]. On the other hand, a stent can be fabricated starting from a planar mesh, which is obtained by appropriately bent wires or laser cut sheets. Thereafter, in order to produce a cylindrical geometry, these meshes require a final joining step, which may consist in mechanical interlocking or welding [14]. Laser welding has been successfully investigated to produce stents made of superelastic materials, i.e. Nitinol [16,17], thanks to its ability to induce limited thermal distortions and sharp heat affected zone. As a result, several patents have been produced, which describe manufacturing methods including welding [18–20]. As far as implants made of bioabsorbable alloys are concerned, little research has been performed up to date. Wang et al. [21,22] produced biodegradable Mg-Zn-Ca stents by photochemical etching of a magnesium foil, which was later rolled into a tube and spot welded. The degradation behaviour of the produced implants was then characterized, but no specific description of the welded areas was reported. In this light, further studies appear to be necessary to better assess the particular features introduced by the presence of a welded zone, for example in the framework of a stent-oriented mesh produced from foil or thin sheet. Moreover, this research thread is susceptible to be expanded to include different alloys, e.g. Fe-based ones, which may exhibit different responses to the process. Besides consolidating knowledge on welding of biodegradable Fe alloys, the reported results may constitute the basis of further developments in the field of laser processing, possibly including surface re-melting.

Due to the lack regarding the effect of laser welding on the degradation behaviour of these alloys, the present work has the goal of investigating, for the first time, the effects of laser welding on Fe-20Mn-0.6C (wt.%) on bulk and surface properties, namely microstructure, mechanical and degradation response, respectively. After having individuated a feasible processing window, the influence of the laser process on the functional properties of such alloy was assessed. In particular, the effect of a different microstructure, arising from the rapid solidification induced by the laser process, on both mechanical response and degradation behaviour was studied.

Summarizing, the present work has been divided into three main parts: (i) identification of the best process condition for obtaining a high quality welded bead; (ii) bulk characterization of the joint and comparison with the base material (microstructural and mechanical properties); (iii) surface characterization, according with degradation testing and evaluation of the reaction products.

2. Materials and methods

2.1. Material production and laser welding process

A Fe-Mn based alloy, namely Fe-20Mn-0.6C wt.%, was melted in a vacuum arc furnace, starting from a Fe-Mn commercial mother alloy (FeMn13 wt.%) and pure Fe and Mn metals. The material was hot rolled at 700 °C and thereafter cold rolled with intermediate annealing steps to a final thickness of 0,6 mm (40% cold working). Finally, 0,6 mm thick samples were annealed for 1 h at 800 °C in Ar atmosphere and then subjected to laser welding in a bead-on-plate configuration. A quasi-continuous wave fibre laser (mod. 300/3000 QCW from IPG Photonics), having a maximum average power of 300 W, was employed. The laser beam was focalized by using a laser head (mod. Fiber Mini from Laser Mech) while a 2D motion stage (mod. PRO165LM from Aerotech) was used; the schematic of the welding process is depicted in Fig. 1a, while the investigated parameters are listed in Table 1.

The present work highlights the differences in mechanical and degradation behaviour between the rolled and annealed material (namely base material) and the samples welded with optimized speed (40 mm/s, namely welded material). The different characterizations are described in the following sections, according with the test system diagram shown in Fig. 1b.

2.2. Microstructural and mechanical characterization

Microstructural characterization was carried out by optical microscopy (Leitz Aristomet) and scanning electron microscopy (SEM, mod. Leo 1413) on polished cross sections, etched with Nital 2% reagent. Compositional analysis was carried out on the three typical zones (base material transition and melted zone) with Energy Dispersive X-ray Spectroscopy (EDS), coupled with a Scanning Electron Microscopy (SEM Leo 1413) and calibrated with a Co reference.

Moreover, diffraction data (CuKα, $\lambda = 1.5418$ Å) were collected on a θ:θ vertical scan Panalytical X'Pert PRO diffractometer, equipped with parallel (Soller) slits – 0.04 rad – and a Real Time Multiple Strip detector in the 20°–120° range. The XRD beam was centered onto the upper surface of the welded bead. Tensile tests were performed, at strain rate of 0.015 min^{-1}, on standard dog-bone specimens (E8/E8M-11 ASTM) by means of an MTS 2/M machine equipped with an extensometer. Welded specimens, carried out with welding speed of 40 mm/s, had the weld bead lying perpendicular to the loading direction.

2.3. Static degradation immersion tests

The tests were carried out accordingly to ASTM G31 standard. Welded (speed 40 mm/s) and base $20 \times 10 \times 2$ mm^3 samples were polished up to 1200 grit before testing; welded samples sported a central weld bead lying parallel to the short side. The samples were weighted, before the immersion, with a 5-digit precision digital balance (Analytical Plus, Ohaus,

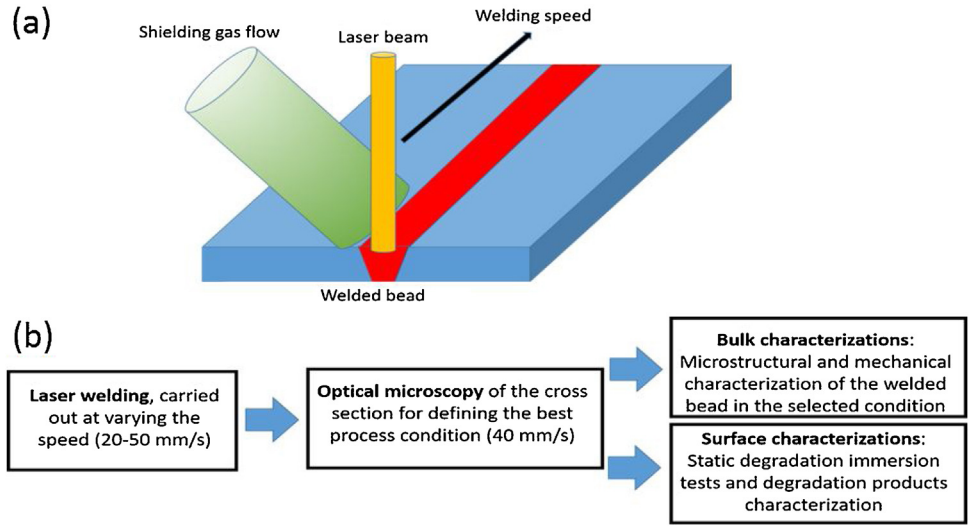

Fig. 1 – Schematic of the welding process (a); test system diagram adopted in the present work (b).

Table 1 – Process parameters adopted for welding Fe-20Mn-0.6C wt.% alloy.

Power [W]	300	Shielding gas	Ar
Speed [mm/s]	20–30–40–50	Shielding gas flow [l/min]	15
Defocused laser spot size [mm]	0.5	Angle of lateral nozzle [°]	35

USA). The degradation test was conducted in modified Hanks' solution (MH), prepared by dissolving 9.7 g of Hanks' balanced salt (H1387, Sigma-Aldrich) in 1.4 L of nanopure water with 14.16 g of HEPES acid (H3375-5000 G, Sigma-Aldrich, USA), 16.65 g of HEPES sodium salt (H7006-500 G, Sigma-Aldrich) [23] and adjusting the pH to 7.4, by addition of 1 M NaOH or 1 M HCl. The solution was filtered under a biological hood with a Steritop® vacuum-driven disposable filtration system (SCGPU02RE, MD Millipore, USA). Each sample was separately immersed in a 100 mL Pyrex sterilized bottle (Corning Incorporated, NY 14831, Germany), with drilled caps (Ø = 1 mm), suspended by a sterile nylon wire in the middle of the solution, before being stored under controlled atmosphere in an incubator at 37 ± 1 °C (p = 1 atm; 85% relative humidity; 5 vol.% CO_2) for 14 days. The minimum "solution volume-to specimen area" ratio was 0.40 mL/mm^2, according to ASTM G31. The extracted samples were cleaned three times for 5 min in a 70% ethanol solution and then weighted. The waste solutions, collected after the test, were centrifuged to separate the degradation products from the supernatant; 20 mL of the supernatant were characterized by microwave plasma atomic absorption emission spectroscopy (MP-AES).

2.4. *Degradation products characterization*

Degraded samples surfaces were analysed by Scanning Electron Microscopy (SEM, JEOL JSM-840A) with a tungsten filament having an acceleration voltage of 15 kV. The microscope was also equipped with a Bruker energy dispersive X-ray spectroscopy (EDS) unit, comprising a Ge detector (Nolan) with a resolution of 115 eV. The chemical composition of the degraded surfaces was also investigated by X-ray photoelectron spectrometer (XPS) PHI 5600-ci (Physical Electronics, Eden Prairie, MN). The base pressure was < 8*10^{-9} Torr. A standard aluminium X-ray source (Al K_α = 1486.6 eV) was used to record survey spectra. The detection angle was set at 45° with respect to the normal of the surface and the analysed area was 0.16 mm^2. Degraded surfaces were analysed by attenuated total reflectance Fourier transform infrared spectroscopy (ATR-FTIR, Agilent Cary 660 FTIR, Agilent Technologies, MN, USA) equipped with a deuterated L-alanine doped triglycine sulphate (DLa-TGS) detector and a Ge coated KBr beam splitter; the acquisition was performed in the wavelength range of 4000 – 400 cm^{-1}, with a resolution of 4 cm^{-1}. MP-AES was performed (Model 4200, Agilent equipment) on the degradation medium, to assess Fe and Mn ions release.

3. Results and discussion

3.1. *Laser welding feasibility, microstructural and mechanical characterization*

The cross sections of the weld beads, performed at varying the speed in the range 20 mm/s to 50 mm/s, are shown in Fig. 2. The energy per unit of volume, called fluence, F (J/mm^3), can be used to describe the energetic contribution during the laser processing:

$$F = \frac{P}{v \cdot t \cdot d}$$

where P, v, t and d indicate power (W), speed (mm/s), thickness of the bead (mm) and spot diameter (mm), respectively. Full penetration beads were realized in the entire range of investigated process speed. However, the shape and the width of the beads were varied, according to the trends reported in Fig. 2a–d. As expected, the increase of the speed caused a progressive decrease of the bead width, according to fluence decrease. In particular, the increase of the speeds causes

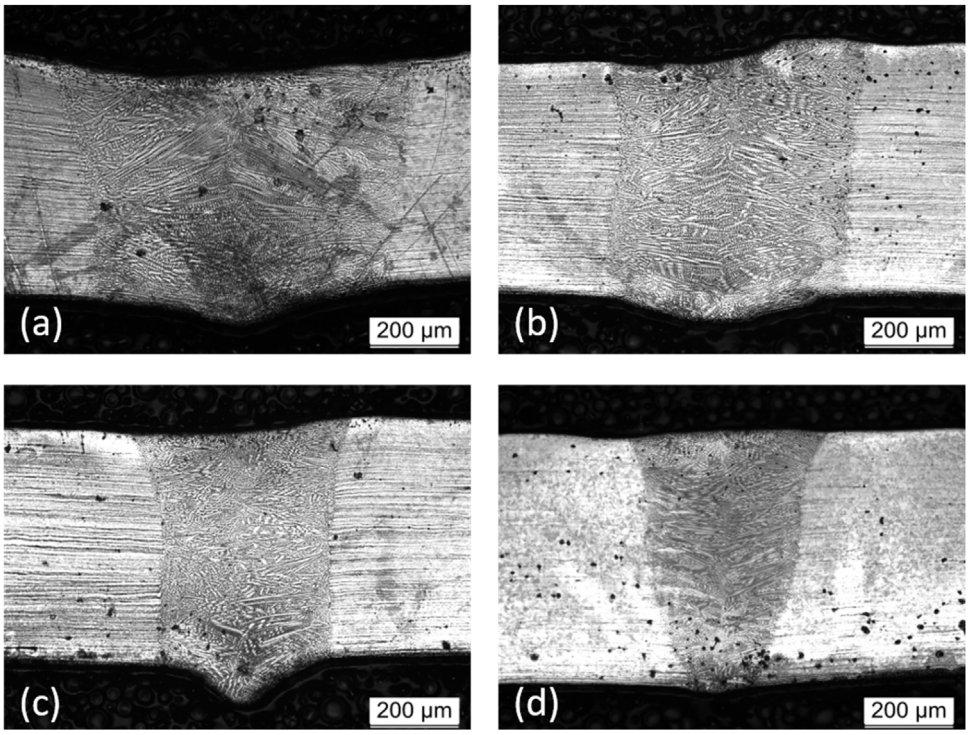

Fig. 2 – Cross sections of Fe-20Mn-0.6C plates welded with speeds 20 mm/s (a), 30 mm/s (b), 40 mm/s (c), 50 mm/s (d).

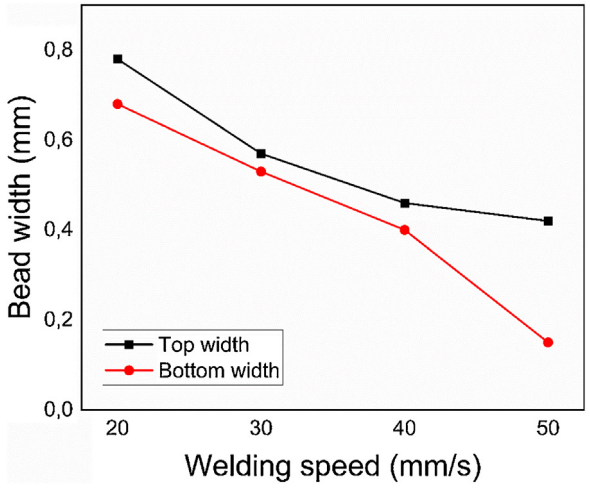

Fig. 3 – Evolution of the top and bottom widths of the welded beads as function of the welding speed.

a decrement of the fluence from 50 J/mm^3, for 20 mm/s, to 20 J/mm^3 for 50 mm/s. Accordingly the resulting bead widths, measured at half sheet thickness, were found to vary between a maximum of 0.72 mm and a minimum of 0.34 mm.

In Fig. 3 the evolution of the top and bottom width of the welded beads, performed by varying the welding speed, is shown. It can be seen that the increase of the speed can promote a decrease of the size of the welded bead, due to the reduction of the fluence transmitted to the material. The identification of the most suitable speed was done, according to the following technological criteria:

(i) the size of the welded bead should not exceed large dimensions, because it would be associated to a large heat affected zone, i.e. large areas where the microstructure of the base material would be strongly modified by intense thermal cycles;
(ii) below or above a "correct" value of process speed, undercuts and drop out are achieved, respectively: these geometrical defects can worsen the mechanical behaviour of the joint;
(iii) in case of large difference between top and bottom width of the welded bead, the bending of the specimen can be induced, making the welding not suitable for high precision components. Therefore, an almost vertical profile of the welded bead is preferred, as to avoid such dangerous bending.

According with these criteria, the most suitable welding speed for a high quality joint was determined to be 40 mm/s (F = 25 J/mm^3), because this value can satisfy the three mentioned points. Moreover, constant width across the section was deemed to be an important feature in order to guarantee stable mechanical properties and uniform advancement of corrosion throughout the part during its degradation. This is the reason why the 50 mm/s condition was discarded, since it granted a slightly lower bead thickness but at the expenses of a uniform thickness across the final welded joint (Fig. 2d).

Therefore, any further characterizations of the welded bead will be performed on samples welded with speed equal to 40 mm/s.

Figs. 4a–c depict cross sections of the samples produced with optimized speed (40 mm/s), lying perpendicular to the rolling direction. The base material consisted of small

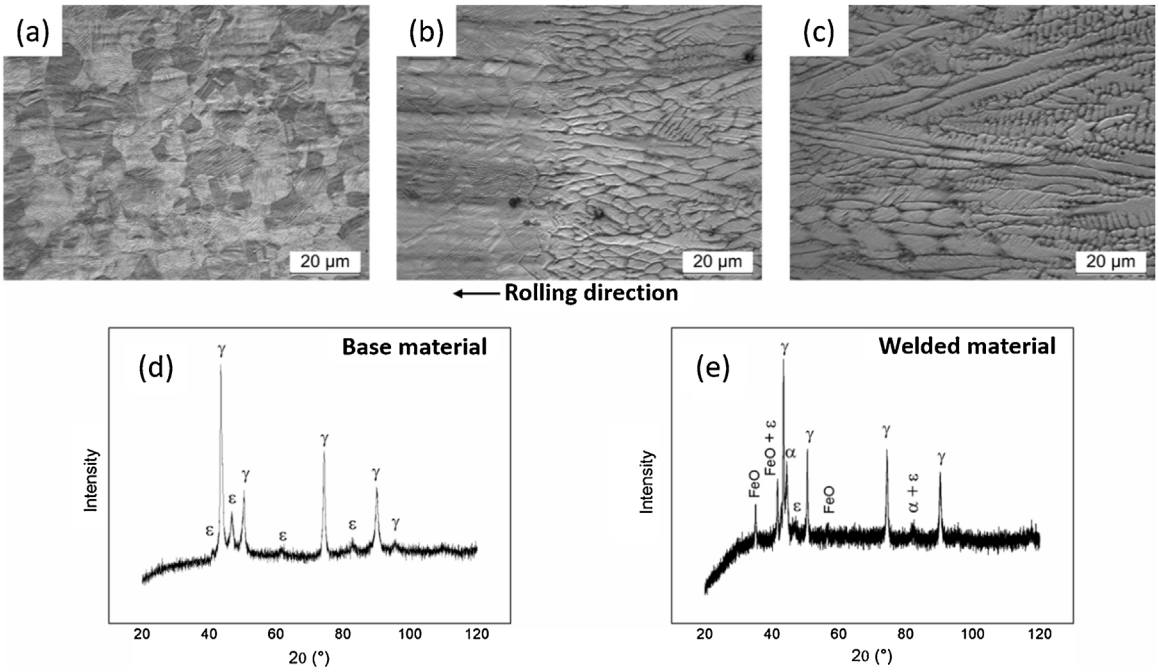

Fig. 4 – Optical micrographs of a welded sample, carried out at 40 mm/s, showing the base metal (a), the transition between base and welded area (b) and the weld bead (c). XRD spectra of the base material (d) and the welded material (e).

Table 2 – EDS compositional analysis through the welded bead, carried out at 40 mm/s.

Areas	Fe [wt.%]	Mn [wt.%]	O [wt.%]
Base material	80.9	19.1	0.0
Transition zone	79.2	20.8	0.0
Welded zone	80.1	19.9	0.0

equiaxed grains, containing a quite high amount of twins, which were generated during the deformation process [11]. On the contrary, the internal part of the weld bead was characterized by a dendritic structure, whose main axis was mainly oriented perpendicularly to the solidification front i.e. towards the base material, due to the rapid solidification. Transition between the two microstructures appeared to be quite abrupt, although no defects or porosities along the interface could be found. Compositional analysis via EDS, carried out on the three zones shown in Fig. 4a–c, highlighted that no evident chemical variation was induced by the laser welding process, carried out by adopting the selected welding speed (see Table 2).

As demonstrated by the XRD spectra reported in Fig. 4d, the base material comprised both face centred cubic austenite (γ) and hexagonal closed packed martensite (ε), which constituted approximately the 75 % and 25 % (wt.%) of the samples, respectively, as computed by Rietveld analysis. The laser-induced melting and solidification (see Fig. 4e) induced two different effects on sample microstructure and chemical composition. First, the rapid cooling from high temperature gave rise to the formation of a further type of martensite, namely the body centred cubic α', detected by XRD (see Fig. 4 e). Secondly, the welding process caused the formation of a superficial FeO oxide layer, due to the interaction of melted material with the surrounding atmosphere. The formation of the FeO can be explained in the following way. It is typical in laser welding to use a shielding gas flow for creating an inert atmosphere, surrounding the liquid pool, for avoiding chemical reactions, like oxidation. Since laser welding is generally carried out with a lateral gas flow (see Fig. 1a), the inert atmosphere is experienced by the liquid pool for a limited time, mainly during its solidification: once solidification is concluded, the solid material continues its cooling down to ambient temperature but the shielding gas action is no more effective, as the nozzle proceeds forward with the laser beam: this means that the solid state cooling is usually not well protected by inert atmosphere. Therefore just the surface of the welded beads can be a little oxidized while the formation of oxides within the interior of the welded bead can be counteracted.

Anyways, the presence of FeO, but not only, was also found in another work, related to laser texturing of Fe-Mn sheets, indicating the high reactivity of this alloy with respect to the environment [27].

Mechanical response in tensile conditions (see Fig. 5a) was assessed in both the base and the welded condition, carried out with welding speed of 40 mm/s. The samples, whose elastic moduli were about 190 GPa, were characterized by marked yielding at 411 MPa for the base material, which slightly decreased to 375 MPa after welding. Ultimate tensile strength was 1095 MPa (base) and 1104 MPa (welded), whereas elongation to failure reached values of 61.3 % and 60.9 % respectively. It shall be underlined that welded samples did not fail in correspondence of the weld bead, thus confirming the extreme soundness of the obtained joining (Fig. 5b). Repeated discontinuous yielding may be noticed in all the reported stress-strain curves (Fig. 5a). This phenomenon

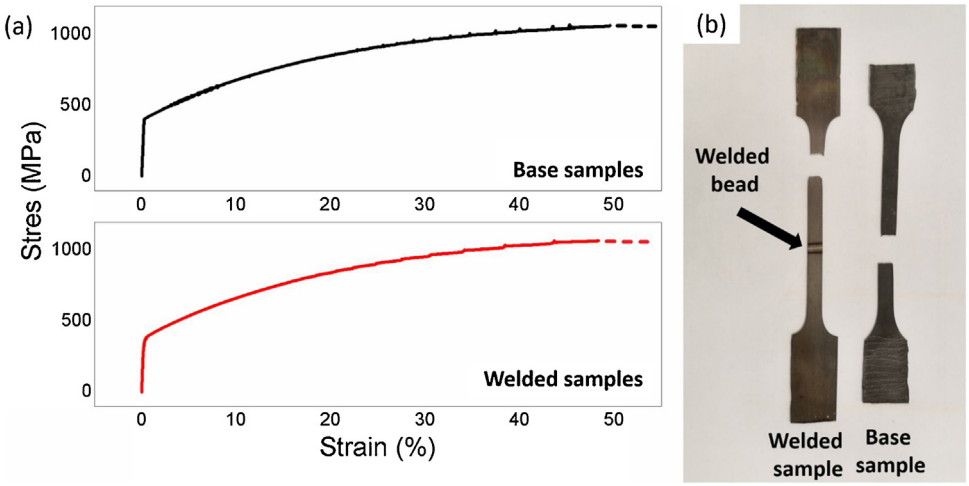

Fig. 5 – Mechanical behaviour of the base material (black curve) and of the welded material at 40 mm/s (red curve) (a); photograph of the specimens after the tensile test (b).

was ascribed to the well-known serrated plastic flow, also called Portevin – Le Chatelier (PLC) effect, which is connected on a microscopic level to the dynamic strain ageing (DSA) mechanism [24,25]. Serrations in stress – strain curves are characteristic of plastic deformation in a specific temperature, strain and strain rate regimes and are connected to attractive interactions between "clouds" of diffusing solute atoms (carbon atoms in the present case) and moving dislocations during deformation. Frequency and type of serrations were not influenced by the welding process.

3.2. *Degradation behaviour*

Fe-20Mn-0.6C wt.% samples, in welded (speed of 40 mm/s) and base conditions, were extracted after 14 days of immersion in MH solution at 37 ± 1 °C (Fig. 6b, d). In both conditions the degradation led to the formation of a superficial conversion coating while just few degradation products, in the form of fine particulate, were finely dispersed in the solution. As visible in Fig. 6a–f, most of the degradation products adhered to the samples surfaces and, in particular, they accumulated along the bead line of the welded sample (Fig. 6b) while appeared more homogenously distributed on the whole surface in the case of base material samples (Fig. 6a).

This indicates that the significant changes in microstructure, due to local and fast melting/solidification induced by laser treatment, affected the degradation response. The weld bead, characterized by a directionally solidified microstructure with fine grains and numerous martensitic plates, appeared as promoter of the degradation process and centre of accumulation for the degradation products (Fig. 4a, c). XPS and FTIR analyses of degraded surfaces gave the same results for both the tested conditions. XPS analyses revealed the presence of C, O and P besides Fe and Mn of the base material. This element amount is compatible with the formation of (Fe, Mn)CO_3. and phosphates layers, as already evidenced by other works [26]. As reported earlier [5], the presence of CO_2 in the testing atmosphere favours the precipitation of carbonates at the metal-solution interface. These precipitates form a compact layer that acts as a protective barrier hindering further degradation. FTIR spectra showed the same peaks for both the samples confirming the presence of phosphates and carbonates forming a passivation layer. Fig. 6 h shows a FTIR spectrum for a typical welded sample. The spectra associated to base material surface after degradation presented the same peaks, with a different intensity. The spectrum was acquired in correspondence of the welding line. The peak at ~ 3300 cm^{-1} could be attributed to the presence of OH- groups, probable due to the presence of adsorbed water on the hygroscopic surface of the material, rich in degradation products. The presence of CO_3^{2-} ions and PO_4^{3-} was consistent with peaks located respectively at ~1250 cm^{-1} and 1000 cm^{-1} [26]. The element maps of Fig. 7 reveal that the degradation products, mainly carbonates and phosphates, are richer in Mn than in Fe. The elements distribution along the welded line is of relevant interest: in fact, even if the degradation products accumulated close to it, the welded line seems to remain exposed to the solution, appearing rich of Fe and Mn of the base material and then promoting new material degradation.

The cross sections of the degraded samples show different corrosion morphologies, which confirm the results described below (Fig. 8a–c). Most of the surface of the base material (Fig. 6 a) was covered by a uniform layer, approximately 2 μm thick, whose composition is compatible with the presence of iron and manganese carbonates ((Fe, Mn)CO_3). On the other hand, localized corrosion appeared in some areas of the base metal (Fig. 8b). A low magnification view of a representative pit is shown in the inset of Fig. 8b, highlighting that some pits can be as deep as 100 μm, and up to 180 μm wide. The layer of degradation products covering these pits was characterized by an inhomogeneous thickness. Furthermore, the degradation layer thickness is generally higher than in flat areas; it is also detached from the underlying metal. EDS analyses confirmed the presence of Fe, Mn and O, compatible the presence of ((Fe, Mn)CO_3), as already found by other authors [26]. Finally, the weld bead was covered mostly with an irregular and weakly-attached attached iron oxide layer, which penetrates in the bulk of the welding following the morphology of

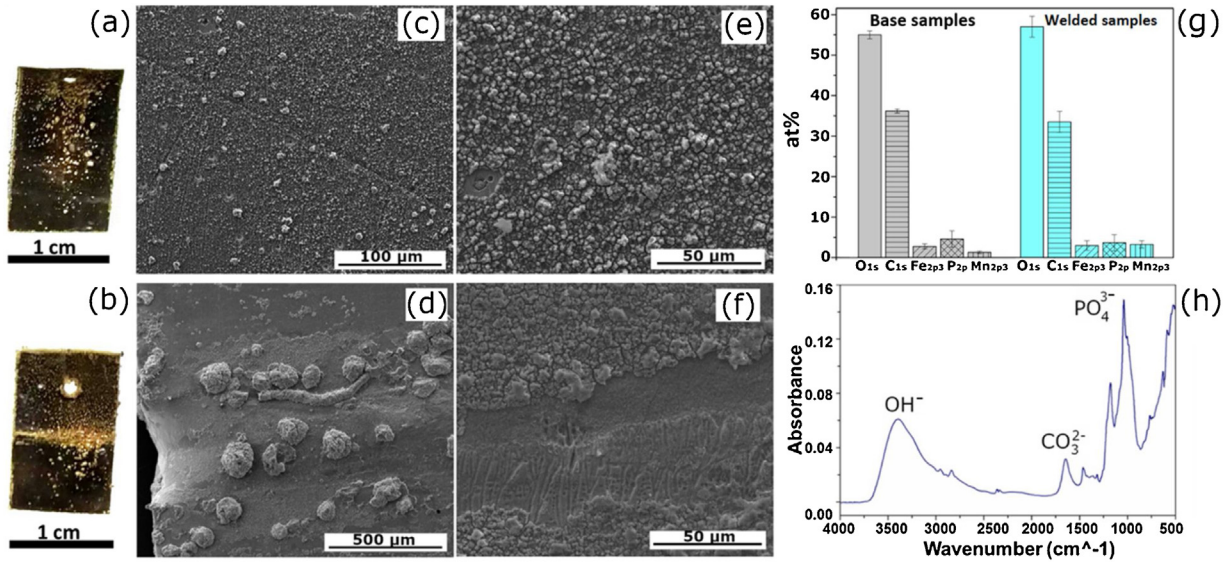

Fig. 6 – Degraded Fe-20Mn-0.6C welded (a), as-received (b) and their respective micrographs (c), (e) and (d), (f). XPS (g) and FTIR (h) characterizations of degraded surfaces.

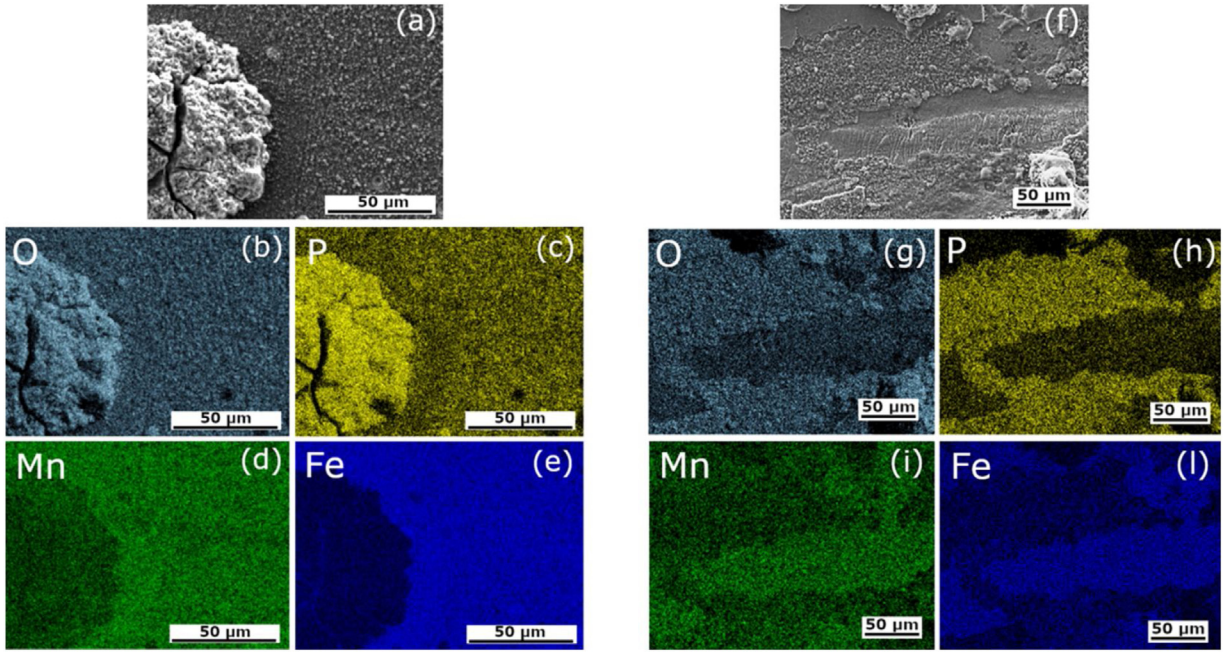

Fig. 7 – Elemental maps of degraded surfaces: central part of as received (a–e) and of welded (f–l) samples after 14 days of immersion in MH solution.

pre-existent dendrites (Fig. 8c). It may be inferred that some form of preferential inter-dendritic corrosion took place, presumably because of the preferential segregation of alloying elements, i.e. mainly Mn, during solidification. Despite this, the weight loss of all the samples after 14 days in modified Hanks' solution was negligible. In particular, it was found that even a slight gain in weight occurred in the case of welded samples (+0,15 %). This indicates that the degradation products did not detach from the surface, in particular from the weld bead using a mechanical cleaning method of mild intensity, such as an ultrasonic bath. MP-AES analysis of the waste medium supernatant (Fig. 8 d) showed that Mn ions concentration was higher than Fe one for both the investigated conditions, that is base and welded material. A slightly higher Mn ions concentration, that is 1.28 ± 0.002 mg/l was found for welded samples. Even if an irrelevant quantitative difference was found in the degradation behaviour of welded alloys and as-received ones immersed 14 days, a massive concentration of degradation products occurred close to the welded line. This phenomenon suggests that the presence of a not

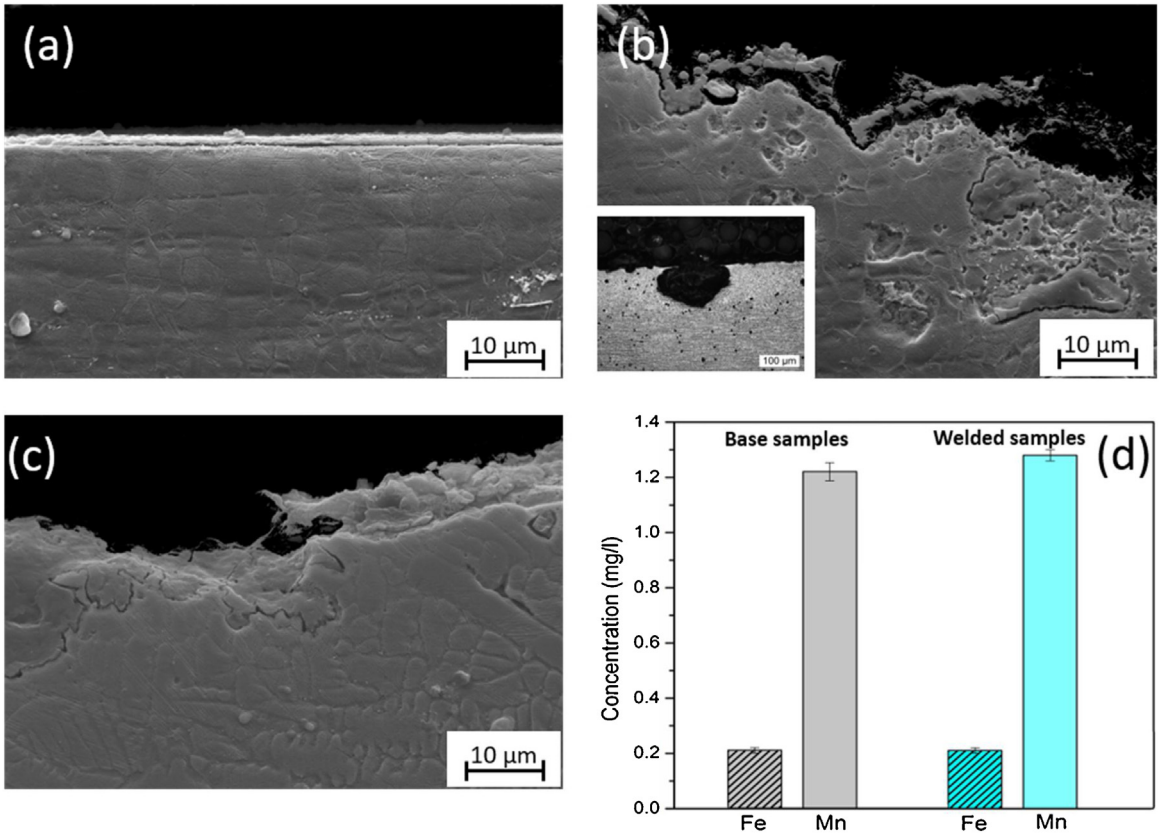

Fig. 8 – SEM micrographs of the cross section of a welded sample after static degradation test: (a) uniform corrosion and (b) pitting corrosion in the as-received sample, (c) corrosion of the weld bead; (d) MP-AES Fe and Mn ionic content of the waste supernatant for the base and welded conditions.

homogeneous microstructure, composed by dendrites, segregation zones and concentration gradients, can play the role of an active electrode during the material degradation processes. Nevertheless, a deeper investigation on degradation behaviour of the welded alloy is pertinent to evaluate how micro-segregation and welding-induced stress can affected the corrosion resistance of the material by increasing the immersion time., as already evidenced for laser welded Fe-30Mn-6Si alloys in a chlorine solution [28].

4. Conclusions

The present study analyses the effect of laser welding in terms of mechanical properties and static degradation behaviour of a Fe-Mn alloy, whose feature targets the good range for degradable biomedical applications. The following conclusions can be highlighted:

- Microstructural changes induced by rapid melting and solidification did not harm the mechanical resistance of the weld bead, which resulted to be equal or even higher than that of the base material.
- As far as the static degradation in pseudo-physiological conditions is concerned, no evident difference in degradation rate and nature of corrosion by-products between the as-received and the welded material was evidenced.
- Therefore, laser welding presently appears to feature promising characteristics, which may allow its widespread application to biodegradable metallic implants. Nevertheless, experimental tests revealed a clear concentration of degradation products at the weld bead, thus suggesting that a deeper understanding of the ongoing degradation pattern is needed.

Declarations of interest

None.

Uncited reference

[15].

Acknowledgements

This work was partially supported by the Natural Science and Engineering Research Council (Innov-College-University-Industry project), as well as the Ministry of Economy and Innovation of the Quebec Province (PSR-SIIRI project). SG was awarded a Postdoctoral Fellowship from the Quebec Excellence Program (2019-2020). The authors would also like to acknowledge Marco Pini and Giordano Carcano from CNR

ICMATE and Niccolò Manzoni from IT IS Badoni for their assistance and support in the experiments.

REFERENCES

[1] Ang HY, Bulluck H, Wong P, Venkatraman SS, Huang Y, Foin N. Bioresorbable stents: current and upcoming bioresorbable technologies. Int J Cardiol 2017;228:931–9, http://dx.doi.org/10.1016/j.ijcard.2016.11.258.

[2] Walker E, Heiden M, Stanciu L. Magnesium, Iron and zinc alloys, the trifecta of bioresorbable orthopaedic and vascular implantation - a review. J Biotechnol Biomater 2015;05, http://dx.doi.org/10.4172/2155-952x.1000178.

[3] Harjanto S, Pratesa Y, Prasetyo Y, Suharno B, Syarif J, Hakim F. Properties of Fe-Mn-C alloy as degradable biomaterials candidate for coronary stent. Adv Mater Res 2013;789:210–4, http://dx.doi.org/10.4028/www.scientific.net/AMR.789.210.

[4] Seol JB, Jung JE, Jang YW, Park CG. Influence of carbon content on the microstructure, martensitic transformation and mechanical properties in austenite/-martensite dual-phase Fe-Mn-C steels. Acta Mater 2013;61:558–78, http://dx.doi.org/10.1016/j.actamat.2012.09.078.

[5] Mouzou E, Paternoster C, Tolouei R, Chevallier P, Biffi CA, Tuissi A, et al. CO2-rich atmosphere strongly affects the degradation of Fe-21Mn-1C for biodegradable metallic implants. Mater Lett 2016;181:362–6, http://dx.doi.org/10.1016/j.matlet.2016.06.017.

[6] Drynda A, Hassel T, Bach FW, Peuster M. In vitro and in vivo corrosion properties of new iron-manganese alloys designed for cardiovascular applications. J Biomed Mater Res Part B Appl Biomater 2015;103:649–60, http://dx.doi.org/10.1002/jbm.b.33234.

[7] Čapek J, Kubásek J, Vojtěch D, Jablonská E, Lipov J, Ruml T. Microstructural, mechanical, corrosion and cytotoxicity characterization of the hot forged FeMn30(wt.%) alloy. Mater Sci Eng C 2016;58:900–8, http://dx.doi.org/10.1016/j.msec.2015.09.049.

[8] Cotes S, Sade M, Guillermet AF. Fcc/Hcp martensitic transformation in the Fe-Mn system: experimental study and thermodynamic analysis of phase stability. Metall Mater Trans A 1995;26:1957–69, http://dx.doi.org/10.1007/BF02670667.

[9] Cotes SM, Fernández Guillermet A, Sade M. Fcc/Hcp martensitic transformation in the Fe-Mn system: part II. Driving force and thermodynamics of the nucleation process. Metall Mater Trans A Phys Metall Mater Sci 2004;35 A:83–91, http://dx.doi.org/10.1007/s11661-004-0111-y.

[10] Sato S, Kwon EP, Imafuku M, Wagatsuma K, Suzuki S. Microstructural characterization of high-manganese austenitic steels with different stacking fault energies. Mater Charact 2011;62:781–8, http://dx.doi.org/10.1016/j.matchar.2011.05.011.

[11] Allain S, Chateau JP, Bouaziz O, Migot S, Guelton N. Correlations between the calculated stacking fault energy and the plasticity mechanisms in Fe-Mn-C alloys. Mater Sci Eng A 2004;387–389:158–62, http://dx.doi.org/10.1016/j.msea.2004.01.059.

[12] Demir AG, Previtali B, Ge Q, Vedani M, Wu W, Migliavacca F, et al. Biodegradable magnesium coronary stents: material, design and fabrication. Int J Comput Integr Manuf 2014;27:936–45, http://dx.doi.org/10.1080/0951192X.2013.834475.

[13] Demir AG, Previtali B, Biffi CA. Fibre laser cutting and chemical etching of AZ31 for manufacturing biodegradable stents. Adv Mater Sci Eng Int J 2013;2013, http://dx.doi.org/10.1155/2013/692635.

[14] Stoeckel D, Bonsignore C, Duda S, Dunitz M. A survey of stent designs. Min Ivas Ther Allied Technol 2002;11:137–47.

[15] Meszlenyi G, Nagy P, Bella S, Dobranszky J. Laser beam cutting and welding of coronary stents. Innov Technol Join Adv Mater 2008:12–3.

[16] Stoeckel D, Pelton A, Duerig T. Self-expanding nitinol stents : material and design considerations. Eur Radiol 2004;14:292–301, http://dx.doi.org/10.1007/s00330-003-2022-5.

[17] Mehrpouya M, Gisario A, Elahinia M. Laser welding of NiTi shape memory alloy: a review. J Manuf Process 2018;31:162–86, http://dx.doi.org/10.1016/j.jmapro.2017.11.011.

[18] Walak SE, US 6,379,392 B1 Welding method; 2002.

[19] Clerc C, Norton P, Leanna ZMG, Roberts G, US 7,993,387 B2 Stent with reduced weld profiles and aclosed-end wire configuration; 2011.

[20] Thompson D, US 9,398,966 B2 Welded stent and stent delivery system; 2016.

[21] Shanov VN, Roy-Chaudhury P, Schulz MJ, Yin Z, Campos-Naciff B, Wang Y, US 9,655,752 B2 Methods for making magnesium biodegradable stents for medical mplant applications; 2017.

[22] Wang J, Giridharan V, Shanov V, Xu Z, Collins B, White L, et al. Flow-induced corrosion behavior of absorbable magnesium-based stents. Acta Biomater 2014;10:5213–23, http://dx.doi.org/10.1016/j.actbio.2014.08.034.

[23] Hermawan H, Dube D, Mantovani D, Le J. Design of a pseudo-physiological test bench specific to the development of biodegradable metallic biomaterials, 4; 2008. p. 284–95, http://dx.doi.org/10.1016/j.actbio.2007.09.012.

[24] Idrissi H, Renard K, Ryelandt L, Schryvers D, Jacques PJ. On the mechanism of twin formation in Fe-Mn-C TWIP steels. Acta Mater 2010;58:2464–76, http://dx.doi.org/10.1016/j.actamat.2009.12.032.

[25] Aydemir B, Zeytin HK, Guven G. Investigation of portevin-le chatelier effect of hot-rolled Fe-13Mn-0.2C-1Al-1Si TWIP steel. Mater. Tehnol 2016;50:511–6, http://dx.doi.org/10.17222/mit.2015.034.

[26] Mouzou E, Paternoster C, Tolouei R, Purnama A, Chevallier P, Dubé D, et al. In vitro degradation behavior of Fe-20Mn-1.2C alloy in three different pseudo-physiological solutions. Mater Sci Eng C 2016;61:564–73, http://dx.doi.org/10.1016/j.msec.2015.12.092.

[27] Donik Č, Kocijan A, Paulin I, Hočevar M, Gregorčič P, Godec M. Improved biodegradability of Fe–Mn alloy after modification of surface chemistry and topography by a laser ablation. Appl Surf Sci 2018;453:383–93.

[28] Lin HC, Lin KM, Chuang YC, Chou TS. Welding characteristics of Fe-30Mn-6Si and Fe-30Mn-6Si-5Cr shape memory alloys. J Alloys Compd 2000;306:186–92, http://dx.doi.org/10.1016/S0925-8388(00)00762-3.